Chapter 1

MODEL DESCRIPTION

The EMEP/MSC-E regional model of heavy metals airborne pollution (MSCE-HM) is a three-dimensional Eulerian type chemical transport model driven by off-line meteorological data. Currently the model is developed and applied for modelling such heavy metals as cadmium (Cd), lead (Pb) and mercury (Hg). Besides, pilot parameterizations for some other metals and metalloids (Cr, Ni, As) are also incorporated. This chapter contains detailed description of the model formulation. It includes definition of the computation domain, model description of the atmospheric transport, chemical transformations and removal processes. Besides, it comprises overview of initial and boundary conditions used for the modelling as well as the procedure of source-receptor relationships calculations.

1.1. Computation domain

The computation domain of the MSCE-HM model is defined on the polar stereographic projection and covers European region along with adjacent territories. The model operates in a regular grid called as the EMEP grid. Characteristics of the projection and the model grid are presented below.

Polar stereographic projection

The polar stereographic projection is a perspective projection of the Earth's surface from one of the poles (the South pole in our case) on a plane perpendicular to the Earth's axis and intersecting the surface at a fixed latitude φ_0. The projection coordinates relates to the Earth's geographical coordinates as follows:

$$\begin{aligned} x &= x_p + R(1+\sin\varphi_0)\tan\left(\frac{\pi}{4}-\frac{\varphi}{2}\right)\sin(\lambda-\lambda_0) \\ y &= y_p - R(1+\sin\varphi_0)\tan\left(\frac{\pi}{4}-\frac{\varphi}{2}\right)\cos(\lambda-\lambda_0) \end{aligned}, \qquad (1.1)$$

where R is the Earth's radius; (x_p, y_p) are the North Pole coordinates;

λ_0 is a rotation angle (longitude parallel to the y-axes of the projection).

Ratio of a small length element on the stereographic projection to the respective element on the Earth's surface (*map factor*) is given by:

$$m = \frac{1+\sin\varphi_0}{1+\sin\varphi}. \qquad (1.2)$$

The polar stereographic projection used in the EMEP has the following parameters:

$$\varphi_0 = 60^\circ\,\mathrm{N}, \qquad \lambda_0 = 32^\circ\,\mathrm{W}$$

More details on the projection characteristics can be found in [*Posch et al*., 2001] or at the EMEP website: www.emep.int.

EMEP grid

The EMEP grid covers the area from approximately 35°W to 60°E and from the North Pole to about 20°N, and includes Europe, partly the North Atlantic and the Arctic oceans, Northern Africa, and part of Middle East (see Fig. 1.1). It has spatial resolution 50×50 km^2 on the projection that corresponds to the same resolution at 60ºN on the Earth's surface. The actual grid size on the Earth's surface slightly decreases southward. The North Pole coordinates in the grid size units are $(x_p,y_p) = (8\Delta x,110\Delta y)$, where $\Delta x = \Delta y = 50$ km. More detailed description of the EMEP grid is available at the *EMEP website* [www.emep.int/grid/].

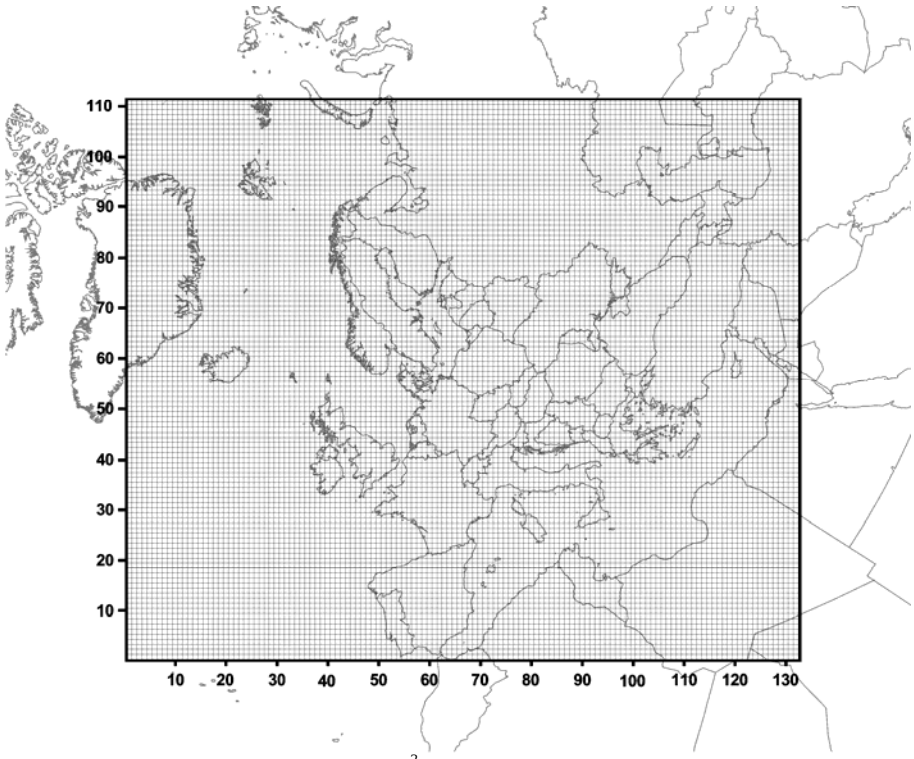

Fig. 1.1. *The EMEP 50×50 km^2 grid*

Vertical structure

The vertical structure of the model is formulated in the sigma-pressure (σ-p) coordinate system [e.g. *Jacobson*, 1999]. The vertical σ-coordinate in this system is defined as:

$$\sigma = \frac{p - p_t}{p^*}, \tag{1.3}$$

where p is local air pressure;

p_t is pressure at the top of the model domain;

$p^* = p_s - p_t$ is difference between the ground surface and model top pressure.

The model domain consists of 15 irregular σ-layers and has a top at p_t = 100 hPa. The layers are confined by surfaces of constant σ and do not intersect the ground topography. The vertical grid structure of the model domain is shown schematically in Fig. 1.2. Characteristics of the σ-layers are presented in Table 1.1.

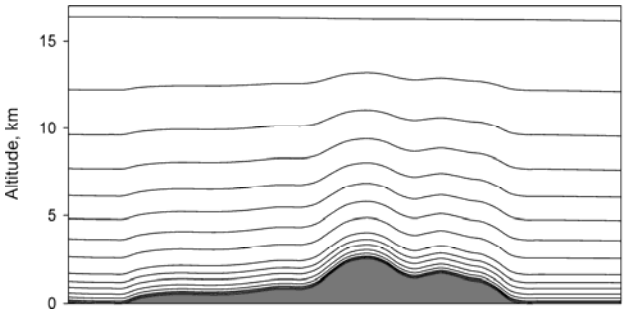

Fig. 1.2. *Vertical grid structure of the model domain. The curves show boundaries of σ-layers*

Table 1.1. *Characteristics of the model σ-layers*

Layer No.	*1*	*2*	*3*	*4*	*5*
Midlevel (σ)	0.995	0.985	0.97	0.945	0.91
Boundaries (σ)	1 - 0.99	0.99 - 0.98	0.98 - 0.96	0.96 - 0.93	0.93 - 0.89
Layer No.	*6*	*7*	*8*	*9*	*10*
Midlevel (σ)	0.87	0.825	0.75	0.65	0.55
Boundaries (σ)	0.89 - 0.85	0.85 - 0.8	0.8 - 0.7	0.7 - 0.6	0.6 - 0.5
Layer No.	*11*	*12*	*13*	*14*	*15*
Midlevel (σ)	0.45	0.35	0.25	0.15	0.05
Boundaries (σ)	0.5 - 0.4	0.4 - 0.3	0.3 - 0.2	0.2 - 0.1	0.1 - 0

The midlevel of the lowest σ-layer approximately corresponds to 37 m. The top of the model domain can be roughly estimated at 15 km.

1.2. Atmospheric transport

The species continuity equation describing the atmospheric transport and dispersion of a pollutant on the stereographic projection with the vertical (σ–p) coordinate has the following form:

$$\frac{\partial}{\partial t}(qp^*) = -m^2\nabla_H \cdot \left(qp^* \frac{\mathbf{V}_H}{m}\right) - \frac{\partial}{\partial \sigma}(qp^*\dot{\sigma}) + \frac{\partial}{\partial \sigma}\left[K_z\left(\frac{g\rho}{p^*}\right)^2 \frac{\partial}{\partial \sigma}(qp^*)\right] + \sum_i S_i \,, \qquad (1.4)$$

where $q = c/\rho$ is a species mass mixing ratio;

c and ρ are the volume concentration and the local air density;

$\dot{\sigma} = d\sigma / dt$ is the vertical scalar velocity in the (σ–p) coordinate;

m is the map factor;

∇_H and $\mathbf{V}_H$ denote horizontal divergence operator and wind velocity respectively;

K_z is the vertical eddy diffusion coefficient; and g is the gravitational acceleration.

In the continuity equation we omitted horizontal eddy diffusion because of the coarse horizontal grid resolution. The local air density ρ at fixed σ-layer is coupled with air temperature T_a and pressure difference p^* through the equation of state:

$$\rho = \frac{\sigma p^* + p_t}{R_a T_a},$$

where R_a is the gas constant for moist air.

The first two terms on the right hand side of the continuity equation describe horizontal and vertical advection of a pollutant in the atmosphere. The third term represents vertical eddy diffusion, the last term describes variety of sources and sinks (emissions, chemical transformations, depositions etc.). The equation is solved by means of the operator-splitting procedure [e.g. *Yanenko*, 1971; *Marchuk*, 1975; *McRae et al.*, 1982]. Following this method, the original equation is approximated by several operator-split equations describing different physical and chemical processes, which are solved sequentially during each time step.

Advection

The sub-equation of the continuity Eq. (1.4) describing horizontal advection has the following form:

$$\frac{\partial}{\partial t}(qp^*) = -m^2\left(\frac{\partial}{\partial x}\left(qp^*\frac{U}{m}\right) + \frac{\partial}{\partial y}\left(qp^*\frac{V}{m}\right)\right), \tag{1.5}$$

where U and V are components of the wind velocity in x and y directions respectively.

The map factor $m = f(x,y)$ is a function of both x and y variables. In order to split the Eq. (1.5) into two one-dimensional equations for x and y directions, respectively, it is convenient to present it in the following form:

$$\frac{\partial \psi}{\partial t} = -\frac{\partial}{\partial x}\left(\psi \hat{U}\right) - \frac{\partial}{\partial y}\left(\psi \hat{V}\right), \tag{1.6}$$

where new variables $\psi = qp^*/m^2$, $\hat{U} = mU$, $\hat{V} = mV$ are introduced.

Eq. (1.6) is solved numerically using Bott flux-form advection scheme with fourth-order area-preserving polynomials [*Bott*, 1989a; 1989b, 1992]. This scheme is mass conservative, positive-definite, monotone, and is characterized by comparatively low artificial diffusion [see e.g. *Dabdub and Seinfeld*, 1994]. In order to reduce the time-splitting error in strong deformational flows the scheme has been modified according to [*Easter*, 1993].

The vertical advection part of Eq. (1.4) is written as follows:

$$\frac{\partial}{\partial t}(qp^*) = -\frac{\partial}{\partial \sigma}(qp^*\dot{\sigma}) \tag{1.7}$$

This one-dimensional advection equation is solved using the Bott scheme with second-order area-preserving polynomials generalized for a grid with variable step $\Delta\sigma$.

Results of basic tests of the model advection scheme are presented in *Annex A*.

Mass consistency

A very important issue for any air quality model is the mass consistency. It means that off-line fields of wind and surface pressure supplied by the meteorological pre-processor should satisfy the continuity equation:

$$\frac{\partial p^*}{\partial t} + m^2 \nabla_H \cdot \left(p^* \frac{\mathrm{V}_H}{m} \right) + \frac{\partial}{\partial \sigma}(p^* \dot{\sigma}) = 0 \,. \tag{1.8}$$

In the terms of an air quality model it implies that the model maintain a uniform mass mixing ratio field of an inert tracer [*Odman and Russel*, 2000]. It can be exactly realized only if the air quality model and a meteorological model supplying input data have the same *discretization*, i.e. grid structure, time step, and finite-difference formulation. However, many transport models (including considered one) have the discretization different from that used in the weather prediction model (WPM) supplying the data. Besides, time resolution of the off-line meteorological data (6 hours for the model involved) is often considerably lower than the model time resolution (10-30 minutes) defined by the numerical stability of the explicit scheme. It requires temporal interpolation of the meteorological data. All mentioned above can lead to a considerable mass inconsistency and the uniform tracer field cannot be maintained. A possible approach to adjust the input meteorological fields to the model discritization is derivation of vertical wind velocity $\dot{\sigma}$ from the continuity Eq. (1.8) at each time step [*Odman and Russel*, 2000].

For the exact mass conservation it is important to apply to solution of Eq. (1.8) the same numerical scheme used for species advection description. The solution is performed in two steps:

Step 1. Solution of the horizontal constituent of the air continuity equation for p^* using Bott advection scheme:

$$\frac{\partial p^*}{\partial t} = -m^2 \nabla_H \cdot \left(p^* \frac{\mathrm{V}_H}{m} \right). \tag{1.9}$$

For the initial condition the surface pressure at the beginning of the time step $(p^*)_t$ is used. As a result a tree-dimensional distribution of the intermediate pressure $(p^*)_{t+\Delta t/2} = f(x,y,\sigma)$ is obtained.

Step 2. Solution of the vertical constituent of the air continuity equation for the vertical velocity:

$$\frac{\partial p^*}{\partial t} = -\frac{\partial}{\partial \sigma}(p^* \dot{\sigma}). \tag{1.10}$$

The intermediate pressure $(p^*)_{t+\Delta t/2}$ from the Step 1 is used as the initial condition; and the surface pressure at the end of the time step $(p^*)_{t+\Delta t} = f(x,y)$ interpolated from the input data is considered as a final condition. The vertical velocity is derived from Eq. (1.10) analytically by inversion of the Bott scheme applied for the vertical transport description.

Details of the vertical velocity calculation procedure are presented in Annex B.

Eddy diffusion

The non-linear equation for vertical eddy diffusion:

$$\frac{\partial}{\partial t}(qp^*) = \frac{\partial}{\partial z}\left[K_z \left(\frac{g\rho}{p^*} \right)^2 \frac{\partial}{\partial z}(qp^*) \right] \tag{1.11}$$

has been approximated by the second-order implicit numerical scheme in order to avoid restrictions of the time step caused by possible sharp gradients of the species mixing ratio. The obtained finite-difference equation is solved by means of the decomposition-backsubstitution method.

1.3. Atmospheric chemistry

Such heavy metals as lead and cadmium and their compounds are characterized by very low volatility. It is assumed in the model that these metals (as well as some others – nickel, chromium, zinc etc.) are transported in the atmosphere only in the composition of aerosol particles. It is believed that their possible chemical transformations do not change properties of their particles-carriers with regard to removal processes.

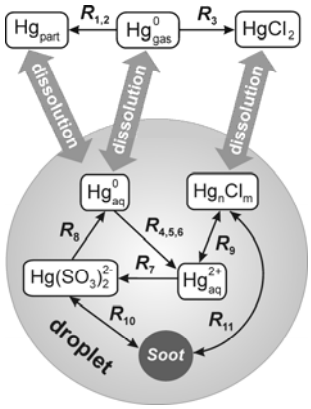

Fig. 1.3. *Scheme of chemical transformations of mercury in the atmosphere*

On the contrary, mercury transformations in the atmosphere include transitions between the gaseous, aqueous and solid phases, chemical reactions in the gaseous and aqueous environment. Hereafter we shall use the term “aqueous phase” for all species dissolved in cloud water and those in composition of solid particles suspended in a droplet. Besides, we shall distinguish three main mercury forms in the atmospheric air: gaseous elemental mercury (GEM), total particulate mercury (TPM) and reactive gaseous mercury (RGM). The last form mostly consists of divalent mercury compounds in gaseous phase, the most typical of which is mercury chloride ($HgCl_2$). The general scheme of mercury transformations in the atmosphere is illustrated in Fig. 1.3.

Inter-phase equilibrium

All gaseous mercury compounds are soluble to some extent in cloud- and rainwater. Size of cloud droplets is small enough to establish the equilibrium between the solution and the gas rather rapidly. The equilibrium described by Henry’s law has pronounced temperature dependence. The expression for the Henry’s law constants (in the form of the ratio of a species concentration in liquid to its air concentration, M·cm^3/molec) are given by:

$$H = A_H T \exp\left[B_H \left(\frac{T_0}{T} - 1 \right) \right], \tag{1.12}$$

where T_0 = 298.15 K; coefficients A_H and B_H for gaseous mercury forms and other gases of interest are presented in Table 1.2.

Table 1.2. *Coefficients of Henry's low constants*

Compound	A_H	B_H	Reference
Hg^0	$1.76 \cdot 10^{-23}$	9.08	*Andersson et al.*, 2004
$HgCl_2$	$1.75 \cdot 10^{-16}$	18.75	*Ryaboshapko et al.*, 2001
O_3	$1.58 \cdot 10^{-24}$	7.8	*Sander*, 1997
$^{\cdot}OH$	$3.41 \cdot 10^{-21}$	17.72	*Jacobson*, 1999
Cl_2	$4.48 \cdot 10^{-16}$ *		*Lin and Pehkonen*, 1999

* - no temperature dependence is available

Besides, we expect that half of particulate mercury mass in cloud- and rainwater is represented by soluble compounds [*Brosset and Lord*, 1991; *Fitzgerald et al.*, 1991; *Lamborg et al.*, 1995]. On the other hand, it is assumed that all mercury mass in the aqueous phase is transformed to the particulate form if the cloud droplet is evaporated.

Gas-phase reactions

One of the most important gas phase reactions is oxidation of elemental mercury by ozone:

$$Hg^0_{(gas)} + O_{3(gas)} \rightarrow Hg(II)_{(part)} + products \tag{1.13}$$

Since, ozone is always in plenty under ordinary atmospheric conditions this second-order reaction is described by a first-order rate expression with the reaction rate constant depending on the reactant concentration:

$$R_1 = -\frac{d[Hg^0_{(gas)}]}{dt} = k_1'[Hg^0_{(gas)}], \tag{1.14}$$

$$k_1' = k_1[O_{3(gas)}], \quad k_1 = A\exp(-E_a/(R_{univ}T))$$

where A = $2.1 \cdot 10^{-18}$ $cm^3/(molec \cdot s)$ [*Hall*, 1995];
E_a = 10.36 kJ/mole;
R_{univ} = 8.31 J/(mole·K);
$[O_{3(gas)}]$ is ozone concentration, $molec/cm^3$.

It is believed that the product of the reaction – mercury oxide is in particulate form due to its poor volatility [*Sommar et al.*, 2001; *Schroeder and Munthe*, 1998].

Recently investigated reaction of mercury oxidation by hydroxyl radical in gaseous phase is expected to be very significant or even prevailing sink of elemental mercury in the troposphere [*Sommar et al.*, 1999; 2001; *Pal and Ariya*, 2004]:

$$Hg^0_{(gas)} + {}^{\bullet}OH_{(gas)} \rightarrow Hg(II)_{(part)} + products, \tag{1.15}$$

$$R_2 = -\frac{d[Hg^0_{(gas)}]}{dt} = k_2'[Hg^0_{(gas)}], \qquad k_2' = k_2[{}^{\bullet}OH_{(gas)}], \tag{1.16}$$

where k_2 = $8.7 \cdot 10^{-14}$ $cm^3/(molec \cdot s)$ [*Sommar et al.*, 2001];
$[^{\cdot}OH_{(gas)}]$ is hydroxyl radical concentration, $molec/cm^3$.

Gas phase oxidation of elemental mercury by chlorine can be noticeable in the ocean boundary layer during nighttime [*Seigneur et al.*, 1994; *Tokos et al.*, 1998; *Ariya et al.*, 2002]:

$$Hg^0_{(gas)} + Cl_{2(gas)} \rightarrow Hg(II)_{(gas)}, \tag{1.17}$$

$$R_3 = -\frac{d[Hg^0_{(gas)}]}{dt} = k'_3[Hg^0_{(gas)}], \qquad k'_3 = k_3[Cl_{2(gas)}], \tag{1.18}$$

where $k_3 = 2.6 \cdot 10^{-18}$ cm^3/(molec·s) [*Ariya et al.*, 2002];
$[Cl_{2(gas)}]$ is chlorine concentration, molec/cm^3.

Aqueous-phase reactions

Dissolved elemental mercury is oxidized by ozone producing mercury oxide *HgO*, which is very short-lived in the liquid phase and is rapidly transformed to the mercury ion Hg^{2+}_{aq}. Thus, the resulting reaction can be written as follows:

$$Hg^0_{(aq)} + O_{3(aq)} \rightarrow Hg^{2+}_{(aq)} + products, \tag{1.19}$$

with the reaction rate expression:

$$R_4 = -\frac{d[Hg^0_{(aq)}]}{dt} = k'_4[Hg^0_{(aq)}], \qquad k'_4 = k_4 H_{O3}[O_{3(gas)}]. \tag{1.20}$$

Here $k_4 = 4.7 \cdot 10^7$ M^{-1}s^{-1} [*Munthe*, 1992];
$[O_{3(gas)}]$ is ozone concentration, molec/cm^3;
H_{O3} is Henry's constant for ozone.

Another important reaction of mercury oxidation in aqueous phase is reaction with hydroxyl radical:

$$Hg^0_{(aq)} + {}^{\bullet}OH_{(aq)} \rightarrow Hg^{2+}_{(aq)} + products. \tag{1.21}$$

Reaction rate expression for this reaction has the following form:

$$R_5 = -\frac{d[Hg^0_{(aq)}]}{dt} = k'_5[Hg^0_{(aq)}]; \qquad k'_5 = k_5 H_{OH}[{}^{\bullet}OH_{(gas)}] \tag{1.22}$$

where $k_5 = 2.4 \cdot 10^9$ M^{-1}s^{-1} [*Gårdfeldt et al.*, 2001];
$[{}^{\cdot}OH_{(gas)}]$ is hydroxyl radical concentration, molec/cm^3;
H_{OH} is Henry's constant for hydroxyl radical.

Elemental mercury in aqueous phase is also oxidized by dissolved chlorine $Cl(I)_{aq}$ with formation of mercury ion Hg^{2+}_{aq}:

$$Hg^0_{(aq)} + Cl(I)_{(aq)} \rightarrow Hg^{2+}_{(aq)} + products, \tag{1.23}$$

$$R_6 = -\frac{d[Hg^0_{(aq)}]}{dt} = k'_6[Hg^0_{(aq)}]\,; \qquad k'_6 = k_6 H_{Cl2}[Cl_{2(gas)}]\,, \tag{1.24}$$

where $k_6 = 2\cdot10^6$ $M^{-1}s^{-1}$ [*Lin and Pehkonen*, 1999];
$[Cl_{2(gas)}]$ is chlorine concentration, molec/cm^3;
H_{Cl2} is Henry's constant for chlorine.

Mercury ion Hg^{2+}_{aq} reacts in the solution with sulphite ions SO_3^{2-} resulting in the formation of mercury sulphite complex $Hg(SO_3)_2^{2-}$ [*Pleijel and Munte*, 1995]:

$$Hg^{2+}_{(aq)} + 2SO^{2-}_{3(aq)} \rightarrow Hg(SO_3)^{2-}_{2(dis)}\,. \tag{1.25}$$

The reaction rate is determined by the air concentration of SO_2 and the cloud water *pH*:

$$R_7 = -\frac{d[Hg^{2+}_{(aq)}]}{dt} = k'_7[Hg^{2+}_{(aq)}]\,, \qquad k'_7 = k_7[SO_{2(gas)}]^2\cdot10^{4\,pH}\,, \tag{1.26}$$

where $k_7 = 1.1\cdot10^{-21}$ s^{-1}, and $[SO_{2(gas)}]$ is in ppbv.

The sulphite complex $Hg(SO_3)^{2-}_{2(dis)}$ is dissociated to mercury sulphite $HgSO_3$, which is unstable, and is readily reduced to $Hg^0_{(aq)}$. Thus, the reduction process can be described as:

$$Hg(SO_3)^{2-}_{2(dis)} \rightarrow Hg^0_{(aq)} + products \tag{1.27}$$

with the reaction rate expression:

$$R_8 = -\frac{d[Hg(SO_3)^{2-}_{2(dis)}]}{dt} = k_8[Hg(SO_3)^{2-}_{2(dis)}]\,, \tag{1.28}$$

where $k_8 = 4.4\cdot10^{-4}$ s^{-1}.

This process increases the amount of dissolved elemental mercury in a droplet hampering further dissolution of gaseous mercury. Hence, the scheme implies negative feedback controlling elemental mercury uptake from the air.

Mercury ion $Hg^{2+}_{(aq)}$ also takes part in a number of reactions leading to the formation of various chloride complexes Hg_nCl_m (R_9). These reversible reactions in the first approximation can be replaced by equilibrium concentrations of free mercury ions and mercury in the aggregate of chloride complexes ($[HgCl^+]$, $[HgCl_2]$, $[HgCl_3^-]$, $[HgCl_4^{2-}]$). The equilibrium ratio of the appropriate mercury concentrations depends upon water content of chloride ion $[Cl^-]$ and is defined as follows [*Lurie*, 1971]:

$$r_1 = \frac{[Hg_nCl_{m(dis)}]}{[Hg^{2+}_{(aq)}]} = \frac{[Cl^-_{(aq)}]}{1.82\cdot10^{-7}} + \frac{[Cl^-_{(aq)}]^2}{6.03\cdot10^{-14}} + \frac{[Cl^-_{(aq)}]^3}{8.51\cdot10^{-15}} + \frac{[Cl^-_{(aq)}]^4}{8.51\cdot10^{-16}}\,. \tag{1.29}$$

The chloride ion concentration in cloud water is taken as $7\cdot10^{-5}$ M [*Acker et al.*, 1998]. Sulphite and chloride complexes in the aqueous phase can be adsorbed and desorbed by soot particles (R_{10}, R_{11}). Comparatively fast equilibrium of these two reverse processes can also be described by means of

"dissolved-to-adsorbed ratio". Based on the appropriate reaction rates it could be taken equal to 0.2 in both cases [*Petersen et al.,* 1998]:

$$r_2 = \frac{[Hg(SO_3)^{2-}_{2(dis)}]}{[Hg(SO_3)^{2-}_{2(soot)}]} = \frac{[Hg_nCl_{m(dis)}]}{[Hg_nCl_{m(soot)}]} \approx 0.2\,. \qquad (1.30)$$

Summary of all chemical transformations of mercury included into the model is presented in Table 1.3.

Table 1.3. *Summary of mercury transformations included into the model*

Reactions and equilibriums	*k* or *H*	Units	Reference
$Hg^0_{(gas)} + O_{3(gas)} \rightarrow Hg(II)_{(part)} + products$	$2.1\cdot10^{-18}\exp(-1247/T)$	$cm^3/(molec\cdot s)$	*Hall*, 1995
$Hg^0_{(gas)} + {}^{\bullet}OH_{(gas)} \rightarrow Hg(II)_{(part)} + products$	$8.7\cdot10^{-14}$	$cm^3/(molec\cdot s)$	*Sommar et al.*, 2001
$Hg^0_{(gas)} + Cl_{2(gas)} \rightarrow Hg(II)_{(gas)}$	$2.6\cdot10^{-18}$	$cm^3/(molec\cdot s)$	*Ariya et al.,* 2002
$Hg^0_{(aq)} + O_{3(aq)} \rightarrow Hg^{2+}_{(aq)} + products$	$4.7\cdot10^{7}$	$M^{-1}s^{-1}$	*Munthe*, 1992
$Hg^0_{(aq)} + {}^{\bullet}OH_{(aq)} \rightarrow Hg^{2+}_{(aq)} + products$	$2.4\cdot10^{9}$	$M^{-1}s^{-1}$	*Gårdfeldt et al.*, 2001
$Hg^0_{(aq)} + Cl(I)_{(aq)} \rightarrow Hg^{2+}_{(aq)} + products$	$2\cdot10^{6}$	$M^{-1}s^{-1}$	*Lin and Pehkonen*, 1999
$Hg^{2+}_{(aq)} + 2SO^{2-}_{3(aq)} \rightarrow Hg(SO_3)^{2-}_{2(aq)}$	$1.1\cdot10^{-21}[SO_{2(gas)}]^{2}\cdot10^{4pH}$ *	s^{-1}	*Petersen et al.,* 1998
$Hg(SO_3)^{2-}_{2(aq)} \rightarrow Hg^0_{(aq)} + products$	$4.4\cdot10^{-4}$	s^{-1}	*Petersen et al.,* 1998
$Hg_nCl_{m(dis)} \leftrightarrow Hg^{2+}_{(aq)}$	$f([Cl])$ **	1	*Lurie*, 1971
$Hg_nCl_{m(dis)} \leftrightarrow Hg_nCl_{m(soot)}$	0.2	1	*Petersen et al.,* 1998
$Hg(SO_3)^{2-}_{2\ (dis)} \leftrightarrow Hg(SO_3)^{2-}_{2\ (soot)}$	0.2	1	*Petersen et al.,* 1998
$Hg^0_{(gas)} \leftrightarrow Hg^0_{(aq)}$	$1.76\cdot10^{-23}T\exp(9.08(T_0/T\text{-}1))$	$M\cdot cm^3/molec$	*Andersson et al.*, 2004
$HgCl_{2(gas)} \leftrightarrow HgCl_{2(aq)}$	$1.75\cdot10^{-16}T\exp(18.75(T_0/T\text{-}1))$	$M\cdot cm^3/molec$	*Ryaboshapko et al.*, 2001
$O_{3(gas)} \leftrightarrow O_{3(aq)}$	$1.58\cdot10^{-24}T\exp(7.8(T_0/T\text{-}1))$	$M\cdot cm^3/molec$	*Sander*, 1997
${}^{\bullet}OH_{(gas)} \leftrightarrow {}^{\bullet}OH_{(aq)}$	$3.41\cdot10^{-21}T\exp(17.72(T_0/T\text{-}1))$	$M\cdot cm^3/molec$	*Jacobson*, 1999
$Cl_{2(gas)} \leftrightarrow Cl(I)_{(aq)}$	$4.48\cdot10^{-16}$	$M\cdot cm^3/molec$	*Lin and Pehkonen*, 1999

* - $[SO_{2(gas)}]$ is in ppbv

** - see Eq. (1.29)

As it was mentioned above one can distinguish three groups of mercury compounds being in equilibrium. The first group (*A*) contains elemental mercury in the gaseous and dissolved phase; the second one (*B*) consists of the mercury sulphite complex both dissolved and on soot particles; and the third group (*C*) includes free mercury ions, mercury chloride complexes dissolved and adsorbed by soot particles and gaseous mercury chloride:

$$A = Hg^0_{(gas)} + Hg^0_{(aq)},$$

$$B = Hg(SO_3)^{2-}_{2(dis)} + Hg(SO_3)^{2-}_{2(soot)}, \qquad (1.31)$$

$$C = Hg^{2+}_{(aq)} + Hg_nCl_{m(dis)} + Hg_nCl_{m(soot)} + HgCl_{2(gas)}.$$

According to this simplified scheme and introduced notations mercury transformations in the liquid phase are described by the following system of the first-order differential equations:

$$\begin{cases} \dfrac{d[A]}{dt} = -\alpha(k_4' + k_5' + k_6')[A] + \beta k_8[B], \\ \dfrac{d[B]}{dt} = -\beta k_8[B] + \gamma k_7'[C], \\ \dfrac{d[C]}{dt} = -\gamma k_7'[C] + \alpha(k_4' + k_5' + k_6')[A]. \end{cases} \quad (1.32)$$

Here $\alpha = H_{Hg}C_w / (\rho_w + H_{Hg}C_w)$ is the fraction of mercury in the *A* group corresponding to the dissolved form; ρ_w is water density; C_w is cloud liquid water content defined as mass of cloud water per unit volume. Parameter $\beta = r_2 / (1 + r_2)$ denotes mercury fraction of the *B* group in the dissolved phase. Value $\gamma = r_2 r_3 / (r_1 r_3 + r_2 r_3 + r_1 r_2)$ is the fraction of mercury in the *C* group corresponding to the mercury ion Hg_{aq}^{2+}. Parameter $r_3 = H_{HgCl2}C_w / (\rho_w + H_{HgCl2}C_w)$ is the fraction of mercury chloride $HgCl_2$ in cloud water. The analytical solution of the equations system with appropriate initial conditions defines mercury evolution in the aqueous phase during one time step.

Mercury depletion events (MDE)

Rapid transformation of elemental mercury to divalent forms with subsequent intensive deposition has been observed in the Arctic during springtime [*Schroeder et al*., 1998; *Berg et al*., 2001; *Lu et al*., 2001; *Lindberg et al*., 2002; *Ebinghaus et al*., 2002]. This phenomenon, which named as *Mercury Depletion Events* (MDE), could be crucial for the Arctic contamination with mercury and adverse impacts on its vulnerable ecosystems. The kinetic mechanism of the phenomenon associated with halogen-related chemistry is not clear understood yet as well as very few measurement data on the reactions kinetics are available. A simplified parameterization of the MDE phenomenon have been developed and used in the sensitivity analysis (*Chapter 3*) to assess the overall effect of the phenomenon on mercury depositions in the Arctic. The main assumptions of the parameterization are presented below:

1. We assume that MDE can occur only over open seawater areas, which were previously covered with ice during winter period. We exclude a possibility of penetration of halogen precursors through ice cover. Hence, we think that MDE can take place over coastal zones of the Arctic Ocean. Only those grid cells are taken into account, which cover both land and see.

2. We suppose that the water surface was previously covered with ice if air temperature in a given point was permanently lower than -3°C during wintertime (assumed seawater freezing point). Then in springtime the temperature became higher than 0°C, and ice melting started. Besides, during springtime ice-drift becomes more intensive and areas of open water appear. Conditionally we “switch on” the MDE module if air temperature during previous 24 hours was higher that 0°C. We understand the conventional character of such a “trigger” because open water can appear in reality at low negative temperatures.

3. We assume that total duration of MDE during springtime in any point does not exceed 4 weeks and MDE takes place every day (instantly at noon) during this period. The MDE module can be “switched on” only within the period from April to June.

4. We believe that during the MDE concentration of elemental mercury near the surface layer drops down from its usual level to 0.1 ng/m^3. Oxidation of Hg^0 leads to the formation of RGM (50%) and Hg_{part} (50%). The oxidized products are partly scavenged from the atmosphere within a given modelling grid cell, partly transported outside it and scavenged later.

5. We accept that the MDE covers the lowest 1-kilometer height layer of the atmosphere. Within this layer the intensity of the phenomenon linearly decreases with height to zero at the top of the layer. Hence, during the MDE elemental mercury has rising profile from 0.1 ng/m^3 at the surface to its usual values at 1 km height. Contrary, oxidized forms have dropping profile from their maximum at the surface to their usual values at 1 km height.

We applied the Arctic definition adopted in the AMAP programme (Fig. 1.4). It covers the terrestrial and marine areas north of the Arctic Circle, north of 62°N in Asia and 60°N in North America, modified to include the marine areas north of the Aleutian chain, Hudson Bay, and parts of the North Atlantic Ocean including the Labrador Sea.

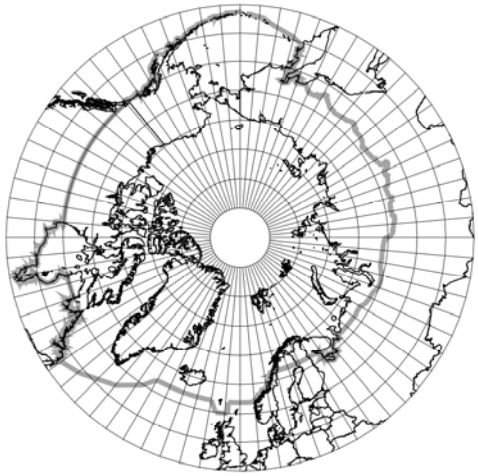

Fig. 1.4. *AMAP Arctic area [AMAP, 1998]*

1.4. Dry deposition

One of the processes accounting for removal of heavy metals from the atmosphere is dry deposition. Heavy metals in aerosol composition or in gaseous form interact with ground surface (buildings, trees, grass, soil, water surface etc.). As a result they stick or react with the surface and are removed from the air. Dry deposition of a substance to a particular surface type *i* is described by the equation:

$$\frac{\partial q}{\partial t} = -\Lambda^i_{dry} q \,, \tag{1.33}$$

where Λ^i_{dry} is the surface dependent dry deposition coefficient, proportional to dry deposition velocity V^i_d :

$$\Lambda^i_{dry} = \frac{V^i_d}{\Delta\sigma_1}\left|\frac{\partial\sigma}{\partial z}\right|, \quad \frac{\partial\sigma}{\partial z} = -\frac{g}{R_a T_a}\left(\sigma_1 + \frac{p_t}{p^*}\right). \tag{1.34}$$

Here $\Delta\sigma_1$ and σ_1 are depth and mid-level of the lowest σ-layer respectively.

The pollutant mixing ratio averaged over a gridcell after the dry deposition is given by:

$$q^{t+\Delta t} = q^t \sum_i f_i \exp(-\Lambda^i_{dry}\Delta t) \tag{1.35}$$

where f_i is area fraction of a surface type *i* in a gridcell and summing is performed over all surface types in the cell.

Commonly the dry deposition velocity is calculated using the resistance analogy [e.g. *Wesely and Hicks*, 2000]. For gases it has the following form:

$$V_d^i = \frac{1}{R_a + R_b + R_c}, \tag{1.36}$$

where R_a is the aerodynamic resistance between a reference height (mid-level of the lowest σ-layer) and the quasi-laminar sub-layer above the surface;

R_b is the quasi-laminar sub-layer resistance;

R_c is the surface resistance to chemical, physical and biological interactions.

Dry deposition velocities of aerosol differ from those of gases (Eq. (1.36)) by absence of the surface resistance and influence of the gravitational sedimentation [*Seinfeld and Pandis*, 1997]:

$$V_d^i = \frac{1}{R_a + R_b + R_a R_b V_g} + V_g, \tag{1.37}$$

where V_g is the gravitational sedimentation velocity.

Aerodynamic resistance

The aerodynamic resistance can be approximated from the similarity theory as [*Jacobson*, 1999]:

$$R_a = \frac{1}{k u_*} \int_{z_{0h}}^{z_{ref}-d} \Phi_h \frac{dz}{z}, \tag{1.38}$$

where k is the von Kármán constant taken as 0.4;

u_* is the friction velocity;

z_{ref} is the reference height (mid-level of the lowest σ-layer);

d is the displacement height;

z_{oh} is the energy roughness length; and Φ_h is the dimensionless potential temperature gradient.

The friction velocity is given by:

$$u_* = k U_{ref} \left(\int_{z_{0m}}^{z_{ref}-d} \Phi_m \frac{dz}{z} \right)^{-1}, \tag{1.39}$$

where U_{ref} is wind velocity at the reference height;

z_{0m} is the roughness length for momentum;

Φ_m is the dimensionless wind shear.

The momentum roughness length z_{0m} for different land cover types along with the displacement heights are given in Table 2.6 (*Chapter 2*). The roughness length for water surfaces is a function of the friction velocity [*Garratt*, 1999]:

$$z_{0m} = \alpha_c u_*^2 / g + 0.11 \nu / u_*, \tag{1.40}$$

where $\alpha_c \approx 0.016$ is the Charnock constant; and ν is the kinematic viscosity of air.

The energy roughness length is expressed through that of momentum for a wide variety of surfaces [*Garratt*, 1999]:

$$\ln\left(\frac{z_{0m}}{z_{0h}}\right) \approx \begin{cases} 2 & \text{rough surface} \\ k(13.6\,\mathrm{Pr}^{2/3} - 12) & \text{water surface} \end{cases}, \tag{1.41}$$

where Pr = $\nu\rho\, c_{pm}/\kappa$ is the Prandtl number;

ρ is air density;

c_{pm} is the specific heat of moist air;

κ is the thermal air conductivity.

The integrals of Φ_h and Φ_m in Eqs. (1.38) and (1.39) are calculated as follows [*Jacobson*, 1999]:

$$\int_{z_{0h}}^{z} \Phi_h \frac{dz}{z} = \begin{cases} \mathrm{Pr}_t \ln\dfrac{z}{z_{0h}} + \dfrac{\beta_h}{L}\left(z - z_{0h}\right) & z/L > 0 \quad (\textit{stable}) \\ \mathrm{Pr}_t\left[\ln\dfrac{(1-\gamma_h\, z/L)^{1/2}-1}{(1-\gamma_h\, z/L)^{1/2}+1} - \ln\dfrac{(1-\gamma_h\, z_{0h}/L)^{1/2}-1}{(1-\gamma_h\, z_{0h}/L)^{1/2}+1}\right] & z/L < 0 \quad (\textit{unstable}) \\ \mathrm{Pr}_t \ln\dfrac{z}{z_{0h}} & z/L = 0 \quad (\textit{neutral}) \end{cases} \tag{1.42}$$

$$\int_{z_{0h}}^{z} \Phi_m \frac{dz}{z} = \begin{cases} \ln\dfrac{z}{z_{0m}} + \dfrac{\beta_m}{L}\left(z - z_{0m}\right) & z/L > 0 \quad (\textit{stable}) \\ \ln\dfrac{(1-\gamma_m\, z/L)^{1/4}-1}{(1-\gamma_m\, z/L)^{1/4}+1} - \ln\dfrac{(1-\gamma_m\, z_{0m}/L)^{1/4}-1}{(1-\gamma_m\, z_{0m}/L)^{1/4}+1} & \\ \quad + 2\tan^{-1}\left(1-\gamma_m\dfrac{z}{L}\right)^{1/4} - 2\tan^{-1}\left(1-\gamma_m\dfrac{z_{0m}}{L}\right)^{1/4} & z/L > 0 \quad (\textit{unstable}) \\ \ln\dfrac{z}{z_{0m}} & z/L = 0 \quad (\textit{neutral}) \end{cases} \tag{1.43}$$

Here $\mathrm{Pr}_t \approx 0.95$ is the turbulent Prandtl number;

$\beta_h = 7.8$; $\gamma_h = 11.6$; $\beta_m = 6.0$; $\gamma_m = 19.3$;

L is the Monin-Obukhov length.

Gridcell averaged values of the Monin-Obukhov length are supported by the meteorological pre-processor (see *Chapter 2*). To obtain values specific for each land cover type we use the following expression for L [*Jacobson*, 1999]:

$$L = -\frac{c_{pd}\,\rho\,\theta_v}{kgH_f}\,u_*^3, \tag{1.44}$$

where c_{pd} is the specific heat of dry air;

θ_v is the potential virtual temperature;

H_f is the vertical turbulent sensible-heat flux.

The Eqs. (1.39) and (1.44) are iterated for u_* and L using the cell averaged values for the initial estimate.

Aerosol deposition

Dry deposition velocities of aerosol is described by Eq. (1.37), where the gravitational sedimentation velocity V_g is given as follows:

$$V_g = \frac{d_p^2 \rho_p g}{18\eta} G_{cunn} . \tag{1.45}$$

Here d_p and ρ_p are the aerosol diameter and density respectively;

G_{cunn} = 1 + Kn (1.249 + 0.42 exp(-0.87 / Kn)) is the Cunningham correction factor [*Jacobson*, 1999];

Kn = 2λ / d_p is the Knudsen number; and λ is the mean free path of air molecules.

In the moist atmospheric air condensation of water vapor on aerosol particles leads to increase of their size. The diameter of an aerosol that is in equilibrium with the air moisture depends upon ambient humidity [*Fitzgerald*, 1975]:

$$d_p = A d_d^B \ ; \qquad A = 1.2 \exp\left(\frac{0.066S}{1.058 - S}\right); \quad B = \exp\left(\frac{0.00077S}{1.009 - S}\right), \tag{1.46}$$

where d_d is the dry diameter of an aerosol;

S is the air saturation ratio.

In this parameterization we expect that the water absorbing mass fraction of the aerosol is equal to unity.

Vegetated surfaces

The size-segregated approach developed for dry deposition to vegetated surfaces is based on theoretical work [*Slinn*, 1982] and fitted to experimental data. Empirical parameterizations based on extensive field measurements [*Ruijgrok et al.*, 1997; *Wesely et. al.*, 1985] are used for selection of the model parameters. A similar approach is suggested by *L.Zhang et al*. [2001]. Following [*Slinn*, 1982] the deposition velocity is expressed in simplified form:

$$V_d^{veg} = \frac{1}{R_a + R_s} + V_g . \tag{1.47}$$

Here R_s is the resistance of the interfacial sub-layer (the layer within and just above the roughness elements) also called as the 'canopy resistance'.

This resistance is calculated as follows:

$$R_s = \frac{U_h}{E u_*^2} , \tag{1.48}$$

where E is the total efficiency of particles collection by the surface;

U_h is the wind velocity at the canopy height H given as:

$$U_h = \frac{u_*}{k} \int_{z_{0m}}^{H-d} \Phi_m \frac{dz}{z} . \tag{1.49}$$

Following *W.G.N.Slinn* [1982] and *L.Zhang et al*. [2001] the collection efficiency has the following form:

$$E = \varepsilon_0 (E_b + E_{in} + E_{im}) r_{off} , \tag{1.50}$$

where E_b, E_{in}, E_{im} are constituents of the collection efficiency from Brownian diffusion, interception and impaction respectively;

r_{off} represents reduction of the efficiency caused by particles bounce-off;

ε_0 is the empirical constant taken from fitting to the experimental data.

The diffusion term is given as [*Slinn*, 1982]:

$$E_b = \mathrm{Sc}^{-2/3} , \tag{1.51}$$

where $\mathrm{Sc} = \nu / D_p$ is the Schmidt number;

D_p is the particle Brownian diffusion coefficient.

We use a generalized form of the impaction term suggested in [*Peters and Eiden*, 1992]:

$$E_{im} = \left(\frac{\mathrm{St}}{\alpha + \mathrm{St}} \right)^{\beta} , \tag{1.52}$$

where $\mathrm{St} = u_* V_g / (g\hat{A})$ is the Stokes number for vegetated surfaces;

$\hat{A}$ is the characteristic collector width given below;

α and β are constants chosen to fit the experimental data.

The interception term is the most uncertain part of the collection efficiency. *W.G.N.Slinn* [1982] parameterized it composing contributions of small (vegetative hairs) and large (grass blades, needles etc.) collectors:

$$E_{in} = F \frac{d_p}{d_p + \check{A}} + (1 - F) \frac{d_p}{d_p + \hat{A}} , \tag{1.53}$$

where $\check{A}$ and $\hat{A}$ are characteristics width of small and large collectors taken as 10 μm and 1 mm respectively;

F and (1-F) are the contributions of these two collector types, where F = 0.01.

The choice of these parameters is arbitrary to some extent since there is no experimental or theoretical data on their values. However, the sensitivity analysis has shown that the interception term is insignificant in comparison with two other terms.

The bounce-off correction factor is taken in the form [*Slinn*, 1982]:

$$r_{off} = \exp(-\gamma \, \mathrm{St}^{\delta}) , \tag{1.54}$$

where γ an δ are the fitting constants.

It is assumed that the particles bounce-off takes place from dry surfaces only. The surface is supposed to be dry if no precipitation occurred during current 6-hours meteorological period for grass and during current and previous periods for forest.

Forests

To evaluate the constants of the deposition scheme described above for tall vegetation (forests) the scheme was fitted to empirical parameterization developed by *W.Ruijgrok et al*. [1997]. This parameterization is based on extensive measurements of dry deposition velocities of aerosol particles over needleleaf and some mixed forests. It takes into account dependence of the dry deposition velocity on the friction velocity and relative humidity of the ambient air. Particles of two size ranges are described: fine fraction with mass median diameter (MMD) = 0.6 μm (NH_4, SO_4, NO_3) and coarse fraction with MMD = 5.12 μm (*Na*). Parameters of dry deposition of different particles in the fine fraction vary insignificantly therefore mean values of the coefficients were used. The fitting constants of the dry deposition scheme obtained for forests are presented in Table 1.4.

Table 1.4. *Empirical constants of the dry deposition scheme for vegetated surfaces*

Constant	Forests	Low vegetation
α	1	1
β	0.5	0.5
γ	2	2
δ	0.25	0.25
ε_0	1.4	0.22
A	–	100

A comparison of the collection efficiency of the Ruijgrok's parameterization with the model scheme is shown in Figs. 1.5 and 1.6 for particles with d_p = 0.6 μm over a wet surface. As seen both schemes give similar functional dependencies on the ambient air relative humidity and the friction velocity. The model scheme predicts more intensive increase of the collection efficiency for relative humidity close to 100%. Similar results are also obtained for a dry surface and for particles with d_p = 5.12 μm.

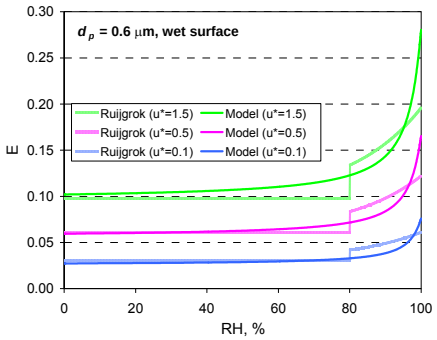

Fig.1.5. *Collection efficiency over forest (wet surface) as a function of the ambient air relative humidity*

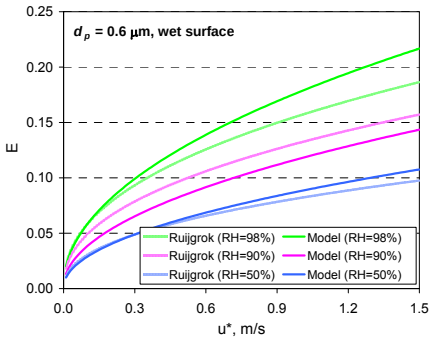

Fig. 1.6. *Collection efficiency over forest (wet surface) as a function of the friction velocity*

Figs. 1.7 and 1.8 shows the dry deposition velocity of aerosol particles over wet and dry forest surface respectively as a function of a particle size. The solid line presents the model scheme, filled squares show the Ruijgrok's parameterization for particles with MMD 0.6 μm and 5.12 μm. As seen from the figures both schemes are in good agreement. The dry deposition velocity of coarse particles over a dry surface is somewhat lower than that over a wet surface because of the bounce-off effect. Besides,

the model scheme was tested using the full set of meteorological data. Fig. 1.9 shows the cumulative distribution function of dry deposition velocity over coniferous forests in Europe obtained for the year 2000 by the model scheme and the Ruijgrok's parameterization. As seen from the figure the results practically coincide.

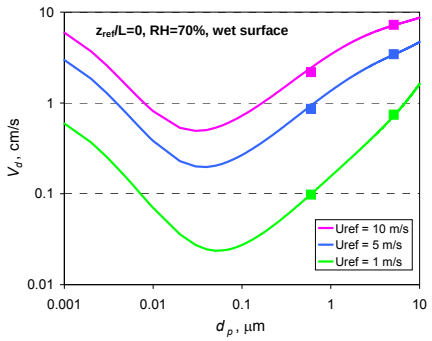

Fig. 1.7. *Dry deposition velocity to forest (wet surface) as a function of a particle size. Solid lines show the model results, the filled squares depict the Ruijgrok's parameterization*

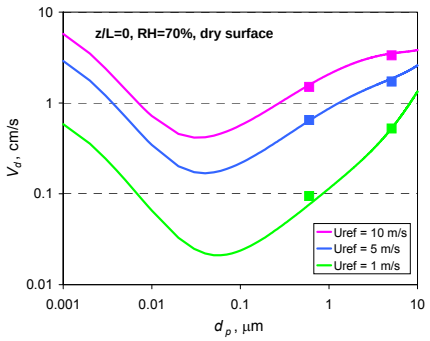

Fig. 1.8. *Dry deposition velocity to forest (dry surface) as a function of particle size. Solid lines show the model results, the filled squares depict the Ruijgrok's parameterization*

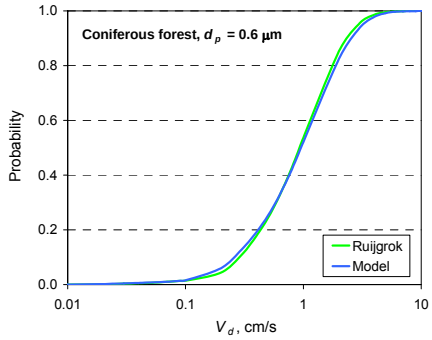

Fig. 1.9. *Cumulative distribution function of dry deposition velocity over coniferous forests in Europe*

Low vegetation

For low vegetation (grassland, crops, wetland etc.) a procedure similar to that described above was used to evaluate the constants of the dry deposition scheme. The scheme was fitted to the empirical parameterization developed from field measurements of particles dry deposition to grass [*Wesely et. al.*, 1985]. The expression for the interfacial sub-layer resistance (1.48) was modified to take into account the atmospheric stability conditions as suggested by *M.L.Wesely et al.* [1985]:

$$R_s = \begin{cases} \dfrac{U_h}{Eu_*^2} & L \geq 0 \\ \dfrac{U_h}{Eu_*^2}\left[1+\left(-\dfrac{\mathrm{A}}{L}\right)^{2/3}\right]^{-1} & L < 0 \end{cases}, \qquad (1.55)$$

where A is a fitting constant.

Values of the fitting constants of the model dry deposition scheme for low vegetation are presented in Table 1.4. Fig. 1.10 shows the comparison of the model scheme for grass with the Wesely's parameterization. As seen the interfacial sub-layer conductivity (reciprocal resistance) given by the Wesely's parameterization lies between those predicted by the model for dry and wet surfaces. The

dry deposition velocity over grass (dry surface) as a function of a particle size is illustrated in Fig. 1.11. The cumulative distribution function of dry deposition velocity over grassland in Europe for conditions of 2000 is shown in Fig. 1.12. As seen from the figure the model somewhat underestimates the Wesely's parameterization for small deposition velocities.

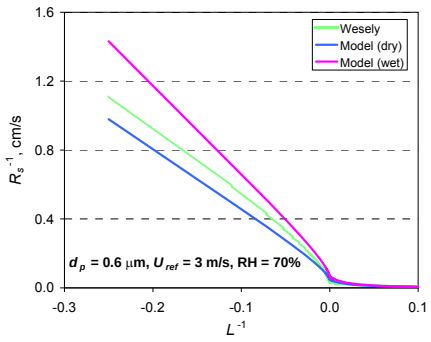

Fig. 1.10. *Reciprocal resistance of the interfacial sub-layer over grass as a function of the stability conditions*

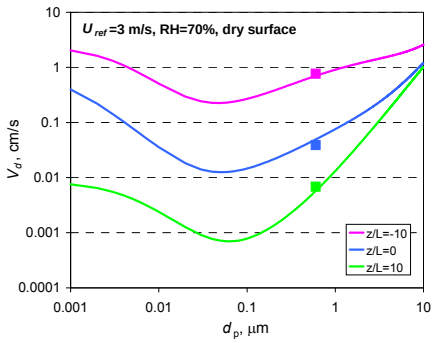

Fig. 1.11.* *Dry deposition velocity to grass (dry surface) as a function of particle size. Solid lines show the model results, the filled squares depict the Ruijgrok's parameterization*

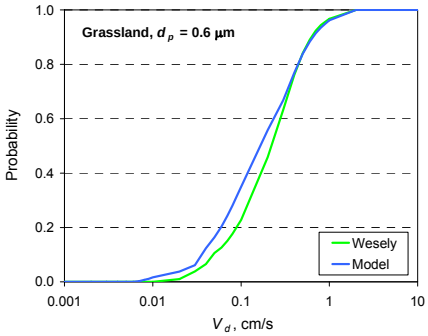

Fig. 1.12. *Cumulative distribution function of dry deposition velocity over grassland in Europe*

Low vegetation covered with snow is considered as non-vegetated surface.

Water surface

The parameterization of dry deposition to water surfaces is based on the approach suggested by *R.M. Williams* [1982] taking into account the effects of wave breaking and aerosol washout by seawater spray. A similar approach was developed in [*Pryor et al.*, 1999]. The modified resistance scheme of aerosol particles dry deposition over water surface is illustrated in Fig. 1.13. Following the procedure from [*Williams*, 1982] one can obtain an expression for the dry deposition velocity:

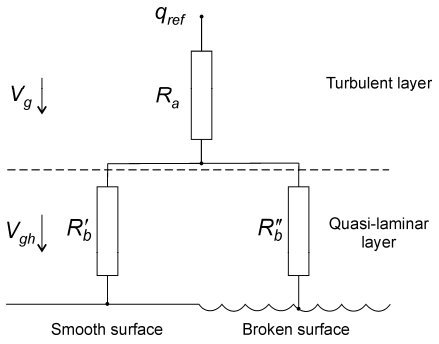

Fig. 1.13. *Resistance scheme of aerosol particles dry deposition over water surface*

$$V_d^{water} = \frac{(1+R_a V_g)(1+R_b V_{gh})}{R_a + R_b + R_a R_b V_{gh}}, \tag{1.56}$$

where V_{gh} is the gravitational sedimentation velocity in the humid quasi-laminar layer near the air-water interface.

The relative air humidity of this layer can be significantly higher that of the turbulent layer. It results in more intensive particle growth. Since due to Raoult's law the relative humidity over salt water cannot exceed 98.3%, the constant value of 98% is accepted in the model for the humid layer. The quasi-laminar layer resistance R_b consists of the resistance over the smooth surface R'_b and the resistance over the broken one R''_b:

$$R_b = \left(\frac{1-\alpha_b}{R'_b} + \frac{\alpha_b}{R''_b} \right). \tag{1.57}$$

Here α_b is the fraction surface area broken due to the wind force [*Wu*, 1979]:

$$\alpha_b = 1.7 \cdot 10^{-6} U_{10}^{3.75}, \tag{1.58}$$

where U_{10} is the wind speed at 10 m height.

The quasi-laminar layer resistance over the smooth surface is determined mostly by the Brownian diffusion and impaction [*Slinn and Slinn*, 1980]:

$$R'_b = \frac{kU_{ref}}{u_*^2}\left(E_b + E_{im}\right)^{-1}, \qquad E_b = \mathrm{Sc}^{-1/2}, \qquad E_{im} = 10^{-3/\mathrm{St}}, \tag{1.59}$$

where the Stokes number for water surfaces is $\mathrm{St} = u_*^2 V_{gh} / (g\nu)$;

the Schmidt number is $\mathrm{Sc} = \nu / D_{ph}$, D_{ph} is the diffusion coefficient in the humid layer.

The broken surface resistance R''_b governed by scavenging of particles due to impaction and coagulation with spray droplets is expected to be quite low. Because of lack of reliable estimates for this resistance a tentative value of 10 s/m [*Williams*, 1982] is used. Fig. 1.14 illustrates the velocity of dry deposition to water surface as a function of particle size for different values of wind speed. The influence of the broken surface resistance on the dry deposition velocity over water surfaces is illustrated in Fig. 1.15. The lowest case corresponds to water surface with no broken area.

Dry deposition to water surface covered with ice is described by the parameterization for barren land presented in the next section.

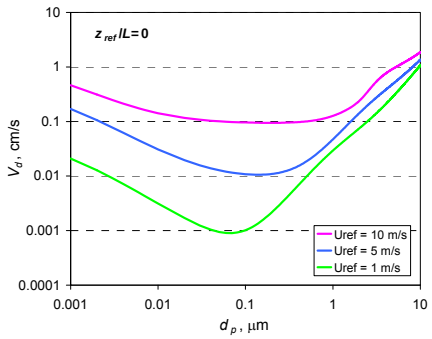

Fig. 1.14. *Dry deposition velocity to water surface as a function of particle size for different values of wind speeds*

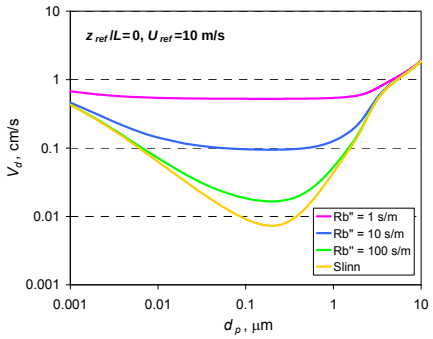

Fig. 1.15. *Dry deposition velocity to water surface as a function of particle size for different values of the broken surface resistance*

Non-vegetated surfaces

The dry deposition to non-vegetated surfaces (deserts, glaciers etc.) is described by Equation (1.37), where the resistance of the quasi-laminar layer has the following form:

$$R_b = \frac{kU_{ref}}{u_*^2}\left(E_b + E_{im}\right)^{-1} \quad , \qquad E_b = \mathrm{Sc}^{-2/3} , \qquad E_{im} = 10^{-3/\mathrm{St}} . \tag{1.60}$$

The Schmidt and the Stokes numbers are Sc = ν / D_p and St = $u_*^2 V_g / (g\nu)$ respectively. The particular case of non-vegetated surfaces is urban area characterized by bluff roughness elements. For urban areas we used a different form of the impaction term E_{im} = St^2 / (400 + St^2) [*Giorgi*, 1986].

Fig. 1.16 shows dry deposition velocities of particles with d_p = 0.6 μm to different land cover categories in the EMEP region calculated for meteorological conditions of 2000. As seen the highest deposition velocities correspond to forests (around 1 cm/s), whereas the lowest – to barren land and permanent ice areas (glaciers) (below 0.01 cm/s on average).

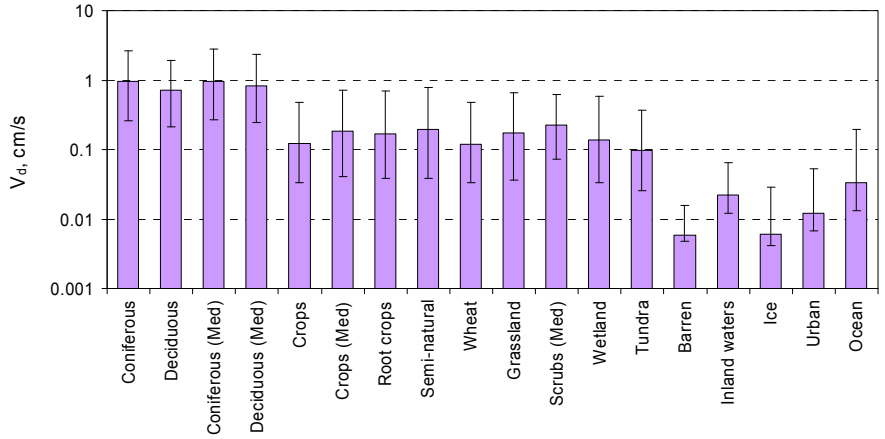

Fig. 1.16. *Dry deposition velocities of particles (d_p = 0.6 μm) to different land cover categories in the EMEP region. Bars show median values of 6-hour averages during 2000. Error bars depict 90%-confidence intervals over the model domain*

The current version of the model describes particles carrying heavy metal as mono-disperse fraction with appropriate MMD: Pb – 0.55 μm, Cd – 0.84 μm, Hg – 0.61 μm [*Milford and Davidson*, 1985].

Reactive gaseous mercury deposition

The dry deposition of reactive gaseous mercury (RGM) is described by Eq. (1.36). The quasi-laminar resistance is given as follows [*Erisman et al.*, 1994]:

$$R_b = \frac{2}{ku_*}\left(\frac{\mathrm{Sc}}{\mathrm{Pr}}\right)^{2/3} , \tag{1.61}$$

where Schmidt number Sc = ν / D_g;

D_g is the molecular diffusion coefficient of RGM.

Since solubility of RGM is similar to those of nitric acid vapor [*Petersen et al.*, 1995] the surface resistance R_c is taken to be zero [*Wesely and Hicks*, 2000].

Dry deposition velocities of RGM to different land cover categories in the EMEP region calculated for meteorological conditions of 2000 are shown in Fig. 1.17. The highest deposition velocities are to forests and urban areas (3 cm/s on average), the lowest velocities are to inland waters (0.5 cm/s).

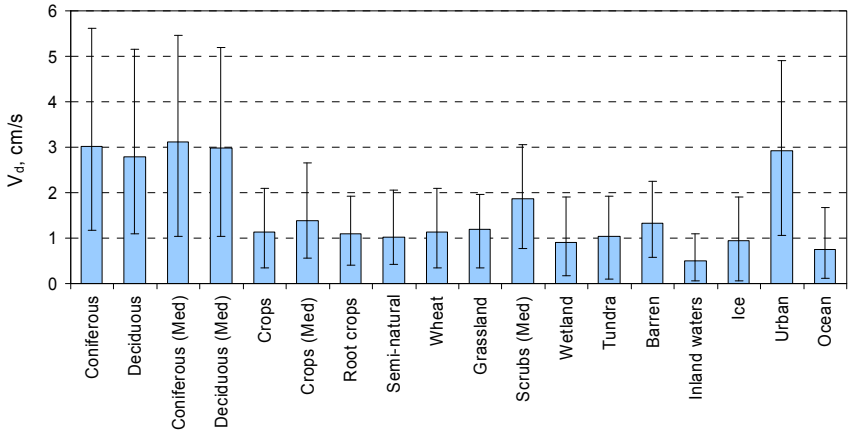

Fig. 1.17. *Dry deposition velocities RGM to different land cover categories in the EMEP region. Bars show median values of 6-hour averages during 2000. Error bars depict 90%-confidence intervals*

Gaseous elemental mercury deposition

Dry deposition of elemental gaseous mercury by various types of underlying surface is not adequately defined yet. Some experts [*US EPA*, 1997] suppose that this type of mercury removal is not an essential sink on a regional and global scale. According to another viewpoint [*Lin and Pehkonen*, 1999] dry uptake of elemental mercury is considered to be the dominating mechanism of mercury removal from the atmosphere. Summarizing available literature data [*Travnikov and Ryaboshapko*, 2002] we adopt the following simplified parameterization of the process. There is no dry uptake of elemental gaseous mercury by water surface and land surface not covered by vegetation. It is also absent during nighttime. Over the vegetated surface during daytime dry deposition velocity is given by:

$$V_d^{veg} = \begin{cases} 0\ , & T_s \le T_0 \\ \mathrm{B}\dfrac{T_s - T_0}{T_1 - T_0}\cos\theta_s\ , & T_0 < T_s \le T_1 \\ \mathrm{B}\cos\theta_s\ , & T_s > T_1 \end{cases}\ , \qquad (1.62)$$

where T_s is the surface temperature, T_0 = 273K and T_1 = 293K;

B is equal to 0.03 cm/s for forests and 0.01 cm/s for low vegetation;

θ_s is the solar zenith angle calculated according to [*Jacobson*, 1999].

Fog deposition

Mercury aqueous forms in fog droplets can be removed from the atmosphere through the fog interaction with the ground surface. The fog dry deposition is described in the model similar to that of aerosol particles with mass median diameter 20 μm.

1.5. Wet deposition

Another important process accounting for heavy metal removal from the atmosphere is wet deposition. Particle-bound heavy metals as well as soluble gaseous species are scavenged form the atmospheric air both in cloud environment and below the cloud base. Wet deposition of a substance is described by the equation:

$$\frac{\partial q}{\partial t} = -\Lambda_{wet} q \,, \tag{1.63}$$

where Λ_{wet} is the wet deposition coefficient depending on the local precipitation rate R_p.

We used the following expression for the wet deposition coefficient based on measurement data:

$$\Lambda_{wet} = A\left(\frac{R_p}{F}\right)^B \,. \tag{1.64}$$

Here A and B are empirical constants;

F is a fraction of the grid cell where precipitation occurs.

We adopt $F = 0.3$ for convective precipitation and $F = 1$ for stratiform one following the discussion in [*Walton et al.*, 1988]. The pollutant mixing ratio averaged over a grid cell after the wet deposition is given by:

$$q^{t+\Delta t} = q^t\left[1 - F\left(1 - \exp(-\Lambda_{wet}\Delta t)\right)\right] \tag{1.65}$$

The model distinguishes in-cloud scavenging (ICS) and below-cloud scavenging (BCS).

In-cloud scavenging

In the cloud environment soluble gases dissolve very quickly in the cloud water coming into the equilibrium with the solution, while aerosol particles are taken up by cloud droplets due to nucleation or impaction scavenging. Further collection of cloud drops by falling raindrops leads to removal of the pollutants from the atmosphere. The efficiency of aerosol scavenging by cloud droplets depends upon the cloud liquid water content (LWC). Fig. 1.18 shows the scavenging efficiencies (i.e. the ratio of aerosol concentration in cloud water to its concentration in interstitial air) for *Pb* and SO_4 measured by *A.Kasper et al.* [1998] as a function of the LWC. For values of the LWC higher than 0.5 g/m^3 the efficiency commonly exceeds 0.8 and it drops down when the LWC become lower 0.1 g/m^3. For the approximation of the dependence we used the following expression:

$$\varepsilon_w = \frac{C_w}{C_w + \varepsilon_{w0}} \,, \tag{1.66}$$

where the liquid water content C_w is in g/m^3;

constant ε_{w0} is equal to 0.1.

Thus for the in-cloud scavenging Eq. (1.65) is transformed to:

$$q^{t+\Delta t} = q^t\left[1-\varepsilon_w F\left(1-\exp(-\Lambda_{wet}\Delta t)\right)\right], \tag{1.67}$$

where the scavenging efficiency ε_w for aerosol particles is defined by Eq. (1.66) and $\varepsilon_w = 1$ for aqueous forms.

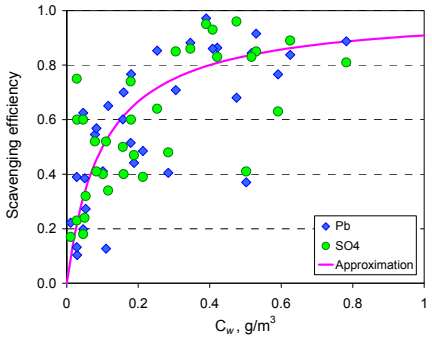

Fig. 1.18. *Efficiency of aerosol scavenging by cloud droplets for lead and sulfate as a function of cloud LWC. Symbols show measurement data from [Kasper et al., 1998], solid line – approximation*

Parameters of the wet deposition coefficient expression (1.64) for in-cloud scavenging estimated or measured by different authors are presented in Table 1.6. Taking into account values in the table and sensitivity calculations we adopted the parameters: $A_{in} = 3\cdot10^{-4}$, $B_{in} = 0.8$ for all heavy metal species incorporated into cloud water.

Table 1.6. *Parameters of the wet deposition coefficient for in-cloud scavenging (A_{in} is in units of s^{-1}; R_p is in units of mm/h)*

Reference	A_{in} ($\times10^{-4}$)	B_{in}	Method
Scott, 1982	3.5	0.78	Calculation
Penner et al., 1991	1.31	1	Estimation *
Brandt et al., 2002	3.36	0.79	Estimation
Andrinache, 2004	3.97	0.81	Measurement **

* - ICS plus BCS of HNO_3
** - Calculations based on measured ICS plus BCS

Below-cloud scavenging

Below the cloud base aerosol particles and soluble gases are collected by falling raindrops and removed from the air. The model parameterization of below-cloud scavenging is mostly based on empirical estimates. Table 1.5 presents parameters of the wet deposition coefficient for BCS of particles and highly soluble gases based on measurement data. As seen different estimates of A_{below} varies roughly from $0.5\cdot10^{-4}$ to $2.5\cdot10^{-4}$ s^{-1}; and B_{below} is within the range 0.62-0.79. There is no principal difference between values of the parameters for sub-micron aerosol particles and highly soluble gases. Basing on the data from the table and the sensitivity runs we adopted the values $A_{below} = 1\cdot10^{-4}$ and $B_{below} = 0.7$ both particle-bound heavy metals and highly soluble gaseous species (RGM).

Table 1.5. *Parameters of the wet deposition coefficient for below-cloud scavenging (A_{below} is in units of s^{-1}; R_p is in units of mm/h)*

Reference	A_{below} ($\times 10^{-4}$)	B_{below}	Method
Ragland and Wilkening, 1983	1.22	0.63	Estimation
Barries, 1985	1	0.67	Measurement
Jylhä, 1991	1	0.64	Measurement
Asman, 1995	0.52-0.99	0.62	Calculation *
Okita et al., 1996	1.38	0.74	Measurement
Brandt et al., 2002	0.84	0.79	Estimation
Andrinache, 2003	0.67 – 2.44	0.7	Calculation **

* - for highly soluble gases

** - theoretical calculations based on measured aerosol size spectra

1.6. Boundary and initial conditions

Modelling of heavy metal airborne pollution requires setting appropriate boundary condition at lateral and upper boundaries of the computation domain. These conditions are aimed at taking into account influence of emission sources located outside the domain. It is particularly important for mercury because of long residence time of this pollutant in the atmosphere. Besides, one-year calculations of mean annual concentrations and deposition fluxes of the pollutant need the model domain to be filled up with the pollutant mass at the start of the modelling. Therefore, one should set some initial concentrations of the pollutant in the atmosphere before the modelling process.

Mercury

Contribution of the intercontinental transport to deposition of mercury in Europe is comparable (up to 40%) with contribution of regional sources [*Ilyin et al.*, 2003]. Therefore, setting the proper boundary concentrations of mercury species at the domain boundaries is principally important for assessment of realistic pollution levels. Besides, it was demonstrated in the sensitivity analysis (*Chapter 3*) that boundary conditions are among the most important parameters determining results of mercury modelling. Available measurement data are too sparse to supply concentrations of mercury along the whole model boundary. To set the boundary conditions adequately we use modelling results obtained with the hemispheric model MSCE-HM-Hem [*Travnikov and Ryaboshapko*, 2002]. Main characteristics of the model are presented in *Annex C*. Both models have similar vertical structures, advection schemes and the same scheme of chemical transformations. Monthly mean concentrations of three atmospheric mercury forms – GEM, TPM, RGM – calculated at the EMEP domain boundaries are used as the regional model boundary conditions. Fig. 1.20 illustrates distribution of gaseous elemental mercury concentration in the vicinity of the model boundary.

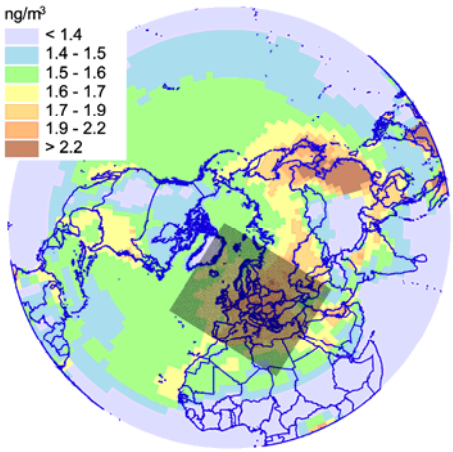

Fig. 1.20. *Distribution of gaseous elemental mercury in the Northern Hemisphere. Rectangular shows the EMEP domain*

As it was demonstrated in aircraft measurements [e.g. *Banic et al.*, 1999] there is no pronounced gradient of GEM up to the upper troposphere. Besides, numerous measurements carried out for last decades [e.g. *Ebinghaus et al.*, 1999] have shown that elemental mercury is more or less uniformly distributed over the Northern Hemisphere. Therefore, we prescribed constant value of GEM concentration at the upper boundary – 0.185 pptv (corresponding to about 1.5 ng/m^3 at 1 atm and 20°C).

Lead

Boundary conditions for lead and cadmium modelling are not so important for the central part of the EMEP region as for mercury because of significantly shorter residence time of these pollutants in the atmosphere. However, background concentrations described by the boundary conditions can have some effect on areas located not far from the model boundaries.

Hemispheric modelling of lead and cadmium airborne transport is not feasible because of lack of up-to-date emission data at the hemispheric or global scale. That is why prescribed boundary concentrations are used for these metals. Measured background concentrations of lead and cadmium in the ambient air vary mostly within the intervals 0.3-3 and 0.02-0.1 ng/m^3, respectively [*Ryaboshapko et al*., 1999; *Kriews and Schrems*, 1998; *Vinogradova*, 2002; *Aas and Breivik*, 2004]. For example, lead concentrations in the northern and northwestern part of the EMEP domain corresponding to the Arctic and the Atlantic Ocean are low because of lack of emission sources nearby (0.3-0.6 ng/m^3). On the other hand, eastern boundary of the model domain lies along the Ural Mountains region, which is characterized by heavy industry and significant emissions and, therefore, relatively high the pollutants concentrations (3.5 ng/m^3 and more).

On the base of measurements data the prescribed values of lead and cadmium boundary concentrations were set at several points of the model boundary (see Fig. 1.21 and Table 1.7). A linear interpolation is applied between the points with different concentration values.

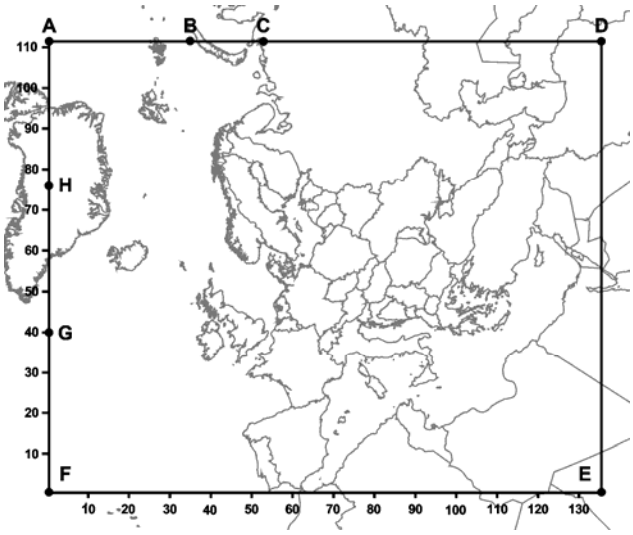

Fig. 1.21. *Scheme of lead and cadmium boundary concentration distribution*

Table 1.7. *Values of the prescribed boundary concentrations*

Boundary points	Concentration, ng/m^3	
	Pb	Cd
A, B, H	0.6	0.02
C	1.5	0.04
D	3.0	0.05
E	2.0	0.05
F, G	1.0	0.03

Besides, when analysing data on air concentrations of lead and cadmium at polar stations Zeppelin (NO42) and Nord (DK10) for many years, distinct seasonal variations were found (Fig. 1.22, 1.23). Since there are no known pollution sources nearby, which can lead to such seasonal variations, the most probably they are caused by the atmospheric transport. In order to take into account this effect, the seasonal variations of boundary concentrations at the northern corner of EMEP domain (intervals AB and AH) were introduced.

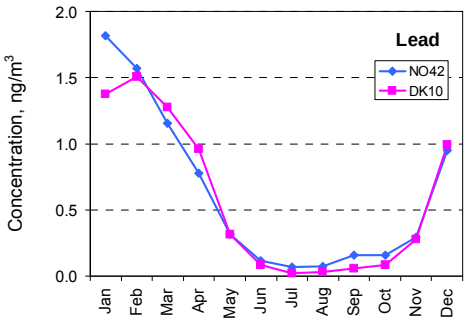

Fig. 1.22. *Seasonal variation of lead at monitoring stations Zeppelin (NO42) and Nord (DK10) averaged over 1994-2002*

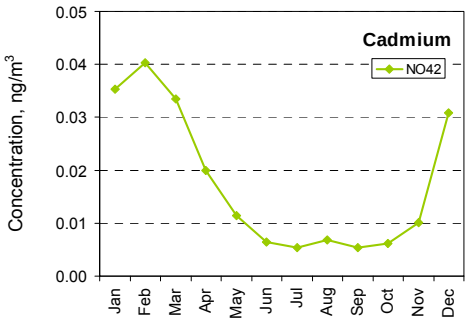

Fig. 1.23. *Seasonal variation of cadmium at monitoring station Zeppelin (NO42) averaged over 1994-2002*

In order to obtain vertical distribution of the boundary concentrations auxiliary model runs for lead and cadmium were performed without any boundary conditions, and average vertical profile for the appropriate region was obtained. Then a factor of the pollutant concentration decrease in comparison with the surface one was calculated for each model layer aloft. The concentration of lead and cadmium at the upper boundary is set to zero.

To fill up the model domain with mass of lead, cadmium and mercury and to achieve the initial concentrations a one-month spin up is performed for the preceding month with the same emissions values and boundary conditions.

1.7. Source-receptor relationships

For the evaluation of source-receptor relationships heavy metal mass emitted from each source (country) is considered separately. To reduce amount of computations and to avoid uncertainties connected with the model non-linearity the computation procedure is organized in such way that all model processes (advection, diffusion, chemistry, deposition etc.) deal with total mass of the pollutant not distinguishing between different sources. Instead, contribution of each source in a gridcell is stored and recalculated after each process modelling. For example, at some time step the contribution of a i^{th} source to the total pollutant mass m in a gridcell is α_i. Then the mass m is changed by value δm_1 due to a process (e.g. advection from the adjacent gridcell) with the fraction of the i^{th} source β_i. The contribution of the i^{th} source to the total pollutant mass in the gridcell ($m + \delta m_1$) at the next time step is given by:

$$\alpha_i' = \frac{\alpha_i m + \beta_i \delta m_1}{m + \delta m_1} . \qquad (1.68)$$

On the other hand, mass removed form a gridcell (e.g. due to dry deposition) related to the i^{th} source is calculated as $\alpha_i \delta m_2$, where δm_2 is the total pollutant mass removed from the gridcell. It should be noted that removal processes decrease the total mass in a gridcell not leading to change in contributions of different sources.

Mass entering the model domain though the boundaries is considered as originated from a separate source to take into account influence of external emission sources.